Is there a unique asteroseismic interior model for the solar-like oscillating KIC 7747078?

Sibel Örtel[1,2]⋆ †, Mutlu Yıldız[1]‡, Zeynep Çelik Orhan[1]§
[1]*Department of Astronomy and Space Sciences, Faculty of Science, Ege University, 35100, İzmir, Turkey*
[2]*Department of Astronomy and Space Sciences, Graduate School of Natural and Applied Sciences, Ege University, 35100, İzmir, Turkey*

Accepted XXX. Received YYY; in original form ZZZ

ABSTRACT
Asteroseismology provides a direct observational window into the structure and evolution of stars. While spectroscopic and photometric methods only offer information about the surface properties of stars, asteroseismology, through oscillation frequencies, provides comprehensive information about the deep stellar interior as well as the surface. The scattering of effective temperature ($T_{\rm eff}$) determined from the spectrum and degeneracy in the Hertzsprung–Russel diagram poses challenges in developing a unique interior model for a single star. Although observational asteroseismic data partially lift this degeneracy, the best model that meets all asteroseismic constraints is not obtained. Most models reported in the literature typically address the large-separation ($\Delta\nu$) constraint between oscillation frequencies, which is a critical issue, especially in post–main sequence stars. Reference frequencies, influenced by helium ionisation zone–induced glitches in oscillation frequencies, are instrumental in refining models. Using the high metallicity derived from the colors of the Kepler Legacy star KIC 7747078, we obtain the mass of models (M) as 1.208 $M_\odot$ and 1.275 $M_\odot$ using the reference frequencies and individual frequencies as constraints, respectively. By applying the χ^2-method using these reference frequencies, $\Delta\nu$, and surface metallicity determined from the spectrum, we develop a unique star model with a mass of 1.171 ± 0.019 $M_\odot$, a radius of 1.961 ± 0.011 $R_\odot$, an effective temperature of 5993 K, an initial metallicity of 0.0121 and an age of 5.15 ± 0.29 Gyr. A significant advantage of this method is that $T_{\rm eff}$ emerges as an output, not a constraint. The mixed-mode oscillation frequencies of this model align well with the observations.

Key words: asteroseismology – star: interior – star: evolution – star: oscillation

1 INTRODUCTION

Asteroseismology is one of the most effective scientific fields that allows the study of astronomical objects (Dupret et al. 2004; Metcalfe et al. 2012; Giammichele et al. 2018). This field examines the oscillation frequencies, in particular those of solar-like oscillating stars, to help us better understand the internal structure and evolution of stars. Since such oscillations have very low amplitude, they cannot be observed well with ground-based telescopes. The CoRoT (Baglin et al. 2006), Kepler (Borucki et al. 2010) and TESS (Sullivan et al. 2015) space telescopes have made it possible to observe the oscillation frequencies of many main-sequence (MS) and evolved stars such as sub-giants (SGs) and red giants (RGs). Since these low-amplitude oscillations are excited by turbulent convection, such oscillations are observed in stars with convective envelopes. These oscillations are either p-mode waves with acoustic properties or mixed modes. The latter behave like acoustic modes in the stellar envelope and like gravity modes in the core, containing important information about the structure of the stellar core. Using the asteroseismic parameters derived from these observational oscillation frequencies, the fundamental properties of these stars can be accurately determined. These asteroseismic parameters are the frequency of maximum amplitude ($\nu_{\rm max}$), large separation ($\Delta\nu$) and small separation ($\delta\nu_{02}$) between oscillation frequencies and the reference frequencies ($\nu_{\rm min}$) attributed to the helium ionisation zone. These parameters and non-astoseismic parameters (like effective temperature ($T_{\rm eff}$), visual magnitude (V) and parallax (π)) are used to determine the fundamental properties of the star, such as age (t), radius (R), mass (M), mean density (ρ) and gravity (g), by constructing interior models using the Modules for Experiments in Stellar Astrophysics (MESA) code (Paxton et al. 2011, 2013, 2015, 2018, 2019; Jermyn et al. 2023). The parameters ρ and g are related to $\langle\Delta\nu\rangle$ (Ulrich 1986) and $\nu_{\rm max}$ (Brown 1991), respectively:

$$\langle\Delta\nu\rangle \propto \sqrt{\frac{M}{R^3}} \propto \sqrt{\rho}, \quad (1)$$

$$\nu_{\rm max} \propto \frac{\rm g}{\sqrt{T_{\rm eff}}}. \quad (2)$$

These relations are very useful to obtain the so-called conventional scaling relations (Kjeldsen & Bedding 1995). According to these relations mass and radius depend on $\langle\Delta\nu\rangle$, $\nu_{\rm max}$, and $T_{\rm eff}$:

$$\frac{M_{\rm sca}}{M_\odot} = \left(\frac{\nu_{\rm max}}{\nu_{\rm max\odot}}\right)^3 \left(\frac{\langle\Delta\nu\rangle}{\langle\Delta\nu_\odot\rangle}\right)^{-4} \left(\frac{T_{\rm eff}}{T_{\rm eff\odot}}\right)^{1.5} \quad (3)$$

⋆ E-mail: sibel.ortel@gmail.com
† ORCID: 0000-0001-5759-7790
‡ ORCID: 0000-0002-7772-7641
§ ORCID: 0000-0002-9424-2339

$$\frac{R_{\rm sca}}{R_\odot} = \left(\frac{\nu_{\rm max}}{\nu_{\rm max\odot}}\right)\left(\frac{\langle\Delta\nu\rangle}{\langle\Delta\nu_\odot\rangle}\right)^{-2}\left(\frac{T_{\rm eff}}{T_{\rm eff\odot}}\right)^{0.5}. \quad (4)$$

Parameters with the symbol $\odot$ represent the solar values. The accepted values are $\langle\Delta\nu_\odot\rangle = 135.1 \pm 0.1$ μHz, $\nu_{\rm max\odot} = 3090 \pm 30$ μHz, and $T_{\rm eff\odot} = 5772 \pm 0.8$ K (Huber et al. 2011; Prša et al. 2016). However, $\nu_{\rm max}$ cannot always be determined easily, and its uncertainty is not always low. For example, hot stars (e.g. Procyon) show double peaks in the power spectrum. Determining which of these peaks should be used in scaling relations is difficult. To solve this problem, Yıldız et al. (2019) derived alternative scaling relations using reference frequencies. If $\nu_{\rm min}$s can be determined from observational frequencies, M and R can be calculated accurately using alternative scaling relations.

The radial order (n) and degree (l) of a mode determine the frequency of the mode (ν_{nl}). While $\Delta\nu = \nu_{nl} - \nu_{n-1,l}$, the term $\delta\nu_{02}$ is the difference between ν_{n0} and $\nu_{n-1,2}$. Here, $\delta\nu_{02}$ is sensitive to the age of the MS stars (Christensen-Dalsgaard 1988). The cavity for the oscillations with $l = 0$ is the whole star, including the centre. However, the turning point of the modes with $l = 2$ is near the boundary of the nuclear core. The mean molecular weight in the core increases as hydrogen is converted into helium. The increase in the mean molecular weight leads to a decrease in the speed of sound. The change in the core region directly affects the frequencies of modes with $l = 0$ but not those of modes with $l = 2$. Therefore, from zero-age main-sequence (ZAMS) to thermal-age main-sequence (TAMS) stars, the nuclear evolution in MS stars reduces $\delta\nu_{02}$.

Solar-like oscillations observed at different evolutionary stages of a star (MS, SG and RG) have motivated many studies on stellar structure and evolution. For example, the mixed modes observed in evolved stars contain information about the internal structure of the star. Using the observed mixed mode frequencies in SG and RG stars, we can obtain strong constraints on the convective core of the stars (Deheuvels & Michel 2011; Arentoft et al. 2017; Montalbán et al. 2013; Çelik Orhan, Yıldız, & Örtel 2023). Noll et al. (2021) obtained strong constraints on the extension of the MS convective core using two g-dominant mixed mode frequencies of the star KIC 10273246. Furthermore, using $\Delta\nu$ and the g-dominant mixed mode, they estimated the core density with a precision of 1% to explain why the high-value core overshooting differs from observations. Similarly, in solar-like oscillating MS stars, convective core constraints are determined using the ratio of small separation to large separation of the radial and dipole modes (Silva Aguirre et al. 2011; Tian et al. 2014; Deheuvels et al. 2016). For evolved stars that show mixed modes, the period spacing parameter ($\Delta\Pi$) determined from the $l = 1$ frequencies of these stars is sensitive to the core region. This parameter can be used to distinguish between the red clump and red giant branch stars, which are difficult to distinguish in the Hertzsprung–Russel (HR) diagram (Mosser et al. 2014; Bedding et al. 2011). In addition, the rotational properties of stars are obtained from solar-like oscillations. Rotation induces rotational splitting of non-radial oscillations, and these splittings are used to obtain the rotation profile of the interior. In studies on RGs and SGs, rotational splitting was used to confirm that the core of the star rotates faster than the outer envelope (Beck et al. 2012; Deheuvels et al. 2012; Ahlborn et al. 2020).

It is possible to construct more than one internal structure model that matches the position of the star in the HR diagram. For MS stars, these models can be distinguished from each other using seismic parameters such as $\delta\nu_{02}$. However, in evolved stars, because of changes in the core, the sensitivity of the parameter to the core structure decreases.

Since other seismic parameters such as $\Delta\nu$ and $\nu_{\rm max}$ are related to the general properties of the star, models that fit different values of M and R can be obtained. Yıldız et al. (2019) examined the discrepancies between the masses $M_{\rm sca}$ and radii $R_{\rm sca}$ obtained from scaling relations and those obtained from internal structure models (mass = $M_{\rm lit}$ and radius = $R_{\rm lit}$) of 83 stars based on asteroseismic data. Interestingly, in the ($\delta M/M = M_{\rm lit} - M_{\rm sca})/M_{\rm sca}$) versus ($\delta R/R = R_{\rm lit} - R_{\rm sca})/R_{\rm sca}$) graph, all stars clustered near the $\delta M/M = 3\delta R/R$ line. This result indicates that asteroseismic internal structure models well fit the observed $\Delta\nu$. However, mass differences can reach up to 20 % and radius differences up to 7 %, indicating that most models reported in the literature lack uniqueness. We already know that equations 3 and 4 require correction (White et al. 2011; Sharma et al. 2016; Yıldız et al. 2016; Yıldız & Örtel 2021). For these reasons, we cannot determine a unique model of an evolved star using only $\Delta\nu$ and $\nu_{\rm max}$.

Another problem encountered when modeling stars is the difficulty in simultaneously fitting $\Delta\nu$ and individual frequencies to observed values. Typically, when a model's $\Delta\nu$ matches the observed value, its individual frequencies do not match, or vice versa. This discrepancy is often attributed to surface effects, leading to the acceptance of one solution over another, which complicates the discussions of model uniqueness.

Unknown chemical composition and age hinder the development of unique interior models. Even if we accurately determine M and R, multiple similar models can emerge with different chemical compositions and ages. Research by Yıldız et al. (2015) demonstrated how reference frequencies vary with chemical compositions in models generated by the ANKİ evolution code (Ezer & Cameron 1965; Yıldız 2011). This indicates that reference frequencies can be used in obtaining a unique model.

In this study, we aim to determine the unique interior model of KIC 7747078 using reference frequencies and asteroseismic ($\delta\nu_{02}$, ν, ν_{min}, etc.) and non-asteroseismic ($T_{\rm eff}$, luminosity (L), R, etc.) observational parameters. Then, the model age and fundamental parameters of the star can be accurately determined. However, many factors influence star evolution. Among them, mass is the best-known factor, which greatly influences star evolution. Similarly, the chemical composition also influences stellar evolution considerably. Depending on the abundance of heavy elements, stellar evolution slows down or speeds up. For example, among two stars with the same mass and different metallicities, the one with a higher metallicity is expected to evolve more slowly. Therefore, in this study, models with various Z_0 and Y_0 values were constructed to understand the effect of chemical composition on the star. We also test the effects of nuclear reaction rates and the chemical mixture of opacity tables for low-temperature regimes.

The rest of this paper is organised as follows: Section 2 presents the observational data of KIC 7747078. Previously published works on this star are presented in Section 3. Section 4 explains the calculation of the mass of the star and the model computation method. The model outputs are discussed in Section 5. Finally, Section 6 presents the conclusions of the study.

2 OBSERVATIONAL DATA

KIC 7747078 is a subgiant star and was observed by the Kepler space telescope. Its non-asteroseismic and asteroseismic observational data compiled from the literature are summarised in Tables 1 and 2, respectively. In Fig. 1, the observational data of KIC 7747078 are plotted on the $\log g - T_{\rm eff}$ diagram. The ZAMS and TAMS are

Table 1. Effective temperature ($T_{\rm eff}$), gravity ($\log g$) and metallicity ([Fe/H]) of KIC 7747078. The references are given in the last column. MZ13 represents Molenda-Zakowicz et al. (2013).

$T_{\rm eff}$(K)	$\log g$(cgs)	[Fe/H]	Reference
5840 ± 60	3.91 ± 0.03	-0.26 ± 0.06	Bruntt et al. (2012)
6114 ± 78	4.37 ± 0.12	-0.11 ± 0.06	MZ13
5994 ± 113	4.04 ± 0.23	-0.19 ± 0.23	MZ13
5918 ± 25	3.94 ± 0.028	-0.14 ± 0.01	Brewer et al. (2016)
5921 ± 60	4.04 ± 0.07	-0.21 ± 0.04	Furlan et al. (2018)
5798.709	3.895	-0.304	Ting et al. (2019)
$5474.1^{+110.7}_{-103.5}$	$3.813^{+0.032}_{-0.033}$	$-0.231^{+0.155}_{-0.152}$	Berger et al. (2020)

Table 2. Frequency parameters of KIC 7747078. Columns include the frequency of maximum amplitude ($\nu_{\rm max}$), large separation ($\Delta\nu$) and references. The maximum difference between $\nu_{\rm max}$ values is ∼5%.

$\nu_{\rm max}(\mu$Hz)	$\Delta\nu(\mu$Hz)	Reference
977	53.7	Appourchaux et al. (2012)
936±32	53.9±0.3	Chaplin et al. (2014)
931±5	53.22±0.01	Li et al. (2020a)

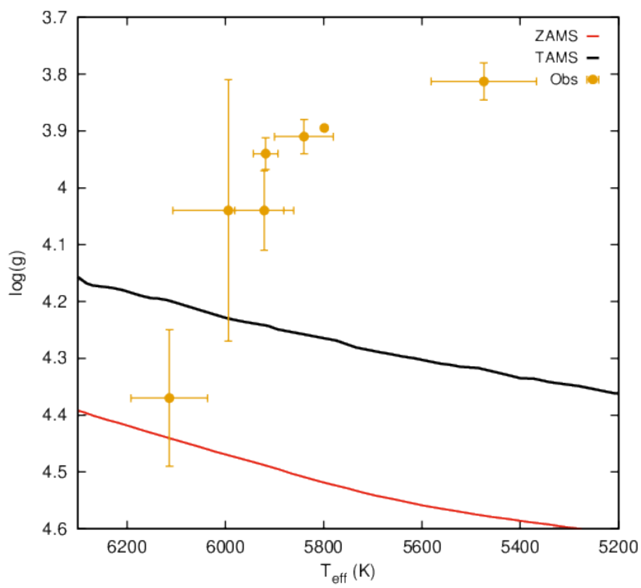

Figure 1. $\log g - T_{\rm eff}$ diagram. The filled yellow circles represent the values reported in the literature for KIC 7747078. Zero-age main-sequence (solid red line) and thermal-age main-sequence (solid black line) are plotted using the models constructed by employing the solar composition (Yıldız 2015).

represented by the red (bottom) and black (top) lines, respectively. The models that form these ZAMS and TAMS lines are constructed with the solar composition derived from the ANKİ code (Yıldız 2015). The filled yellow circles show the observational data for KIC 7747078 in Table 1. The visual magnitude (V) of the star is taken as 9.52 mag from the SIMBAD database. The distances (d) of the star determined from Gaia DR2 and EDR3 data are 180.1 and 179.958 pc, respectively (Gaia Collaboration et al. 2018, 2021). The values of $T_{\rm eff}$ (5474−6114 K), $logg$ (3.81−4.37) and [Fe/H] (−0.30 to −0.11 dex) are reported in previous studies (Bruntt et al. 2012; Molenda-Zakowicz et al. 2013; Brewer et al. 2016; Furlan et al. 2018; Ting et al. 2019; Berger et al. 2020). There is a very large scatter in the $\log g$ and $T_{\rm eff}$ values in particular. While $\log g$ can be calculated using equation 2, the scatter in $T_{\rm eff}$ raises concerns about its use as a direct constraint for developing interior models (Section 5).

The observational asteroseismic parameters $\nu_{\rm max}$ and $\Delta\nu$ are reported in three previous studies (Appourchaux et al. 2012; Chaplin et al. 2014; Li et al. 2020a). The values of $\nu_{\rm max}$ and $\Delta\nu$ are 931−977 and 53.2−53.9, respectively. Finally, the observed frequencies of the star are taken from Appourchaux et al. (2012) and Li et al. (2020a). Observational frequencies are listed in the first two columns in Table 4.

3 PREVIOUS MODEL STUDIES ON KIC 7747078

KIC 7747078 has left the MS phase and is in the SG phase. This star has been widely studied. Chaplin et al. (2014) analysed more than 500 MS and SG stars, including KIC 7747078. They derived the fundamental parameters of KIC 7747078 from two different data sets using Kepler's asteroseismic data. In the first method, they used $T_{\rm eff} = 5418 \pm 176$ K and $[{\rm Fe/H}] = -0.20 \pm 0.30$, as determined by the infrared flux method (IRFM), to estimate M, R and t as $1.04^{+0.12}_{-0.11}$ M$_\odot$, 1.89 ± 0.08 R$_\odot$ and $8.9^{+3.2}_{-2.3}$ Gyr, respectively. In the second method, they used the spectral $T_{\rm eff} = 5840 \pm 84$ K and [Fe/H]= 0.26 ± 0.09 values obtained by Bruntt et al. (2012). The values of M, R and t determined by the second method are 1.10 ± 0.06 M$_\odot$, 1.93 ± 0.04 R$_\odot$ and 6.5 ± 0.8 Gyr, respectively.

On the other hand, Metcalfe et al. (2014) analysed 42 solar-like oscillating MS and SG `Kepler` targets using spectroscopic and asteroseismic data. They constructed interior models of the stars using the Asteroseismic Modelling Portal. They obtained the following results for KIC 7747078: $M = 1.06 \pm 0.05$ M$_\odot$, $R = 1.889 \pm 0.023$ R$_\odot$ and $t = 6.26 \pm 0.92$ Gyr. They also estimated the abundance of heavy elements (Z), helium abundance (Y_0) and mixing length parameter (α). The model input parameters are $Z = 0.0103 \pm 0.0019$, $Y_{\rm i} = 0.271 \pm 0.020$ and $\alpha = 1.76 \pm 0.20$.

Yıldız et al. (2019) analysed the *Kepler* and *CoRoT* stars in the RG, SG and MS evolutionary phases and derived a new scaling relation from the interior models. In addition, they used the reference frequencies ($\nu_{\rm min0}$ and $\nu_{\rm min0}$) to calculate the mass ($M_{\rm sis0}$ and $M_{\rm sis1}$) and radius ($R_{\rm sis0}$ and $R_{\rm sis1}$). The fundamental parameters they determined for this star are as follows: $M_{\rm sca} = 1.12 \pm 0.16$ M$_\odot$, $R_{\rm sca} = 1.94 \pm 0.10$ R$_\odot$, $M_{\rm sis0} = 1.10 \pm 0.02$ M$_\odot$, $M_{\rm sis1} = 1.12 \pm 0.02$ M$_\odot$, $R_{\rm sis0} = R_{\rm sis1} = 1.95 \pm 0.01$ R$_\odot$. They also determined the age and initial metallicity as $t_{\rm sis} = 4.00 \pm 0.20$ Gyr and $Z_0 = 0.0128 \pm 0.0007$, respectively.

Finally, Li et al. (2020b) modelled 36 Kepler SG stars and determined their ages. The mass, radius, luminosity and age estimates for KIC 7747078 are 1.11 ± 0.06 M$_\odot$, 1.92 ± 0.03 R$_\odot$, 4.00 ± 0.25 L$_\odot$ and 6.22 ± 0.76 Gyr, respectively. The results obtained by Çelik Orhan, Yıldız, & Kayhan (2021) are similar to the results reported by Li et al. (2020b).

4 METHODS

4.1 Computation of mass and radius

Stellar mass is one of the most influential parameters for stellar structure and evolution. Therefore, it is crucial to determine the mass accurately. Different methods can be used to determine the mass of solar-like oscillating stars. For single stars, despite some uncertainty, stellar mass is calculated by the classical method based on parallax (π) (see below). To estimate the mass of a star using this method, we need distance (d_π), magnitude, [Fe/H], $T_{\rm eff}$ and $\log g$ data. The Gaia mission has provided data on the distance values of most of the Kepler target stars. Since KIC 7747078, too, is observed by Gaia, the fundamental parameters can be calculated using the classical method.

The first step in this method is to calculate the absolute magnitude (M_V). M_V is obtained using d_π and the apparent magnitude V. In the next step, the bolometric magnitude ($M_{\rm bol}$) is obtained from the absolute magnitude and bolometric correction tables (Lejeune, Cuisinier & Buser 1998). Then, L of KIC7747078 is calculated from $M_{\rm bol}$. Then, R_π is estimated as follows:

$$\frac{R_\pi}{R_\odot} = \left(\frac{L}{L_\odot}\right)^{0.5} \left(\frac{T_{\rm eff\odot}}{T_{\rm eff}}\right)^2. \quad (5)$$

Finally, using the g value determined from the spectral or asteroseismic $\log g$ and the calculated R_π value, we estimate the mass (M_π) as follows:

$$\frac{M_\pi}{M_\odot} = \left(\frac{g}{g_\odot}\right) \left(\frac{R}{R_\odot}\right)^2. \quad (6)$$

Many observational parameters influence the uncertainty in M_π. The accurate estimation of M_π depends on the accuracy of observational $\log g$.

The asteroseismic parameter $\langle\Delta\nu\rangle$ can be used to test the accuracy of the estimated mass calculated by this method. Toward this end, we construct evolutionary models of different masses. L, R and $T_{\rm eff}$ of the models are fitted to the observed values. For a given value of R, changing the M value causes a change in the mean density. Models with different masses have different $\langle\Delta\nu\rangle$ values ($\langle\Delta\nu_{\rm mod}\rangle$). By comparing $\langle\Delta\nu\rangle$ and $\langle\Delta\nu_{\rm mod}\rangle$, we can determine the model with the more appropriate mass.

The compiled observational data of KIC7747078 are listed in Table 1. Different observational data yield different values for the fundamental parameters of the star. The evolutionary tracks of the models constructed using these fundamental parameters also differ from each other. The results of the constructed models are discussed in Section 5.

The second method is based on the computation of $M_{\rm sca}$ and $R_{\rm sca}$ from equations (3) and (4), respectively. KIC 7747078 is an SG star; however, equations (3) and (4) are scaled to an MS star, namely the Sun. Therefore, more general forms of equations (3) and (4) are required for the evolved stars (White et al. 2011; Yıldız & Örtel 2021; Yıldız 2023). In this method, we use $R_{\rm sca}$ instead of R_π in the classical method. Since the uncertainty in $M_{\rm sca}$ is much greater than that in $R_{\rm sca}$, we construct interior models for KIC 7747078 with the same radius but different masses. Then, we compute the adiabatic oscillation frequencies and obtain the $\langle\Delta\nu_{\rm mod}\rangle$ and $\nu_{\rm min}$s values of each model. By comparing the model and the observational values of $\langle\Delta\nu\rangle$ and $\nu_{\rm min}$s, we can find the suitable value of $M_{\rm mod}$ for a given value of $R_{\rm sca}$. For fine-tuning $\langle\Delta\nu\rangle$ and $\nu_{\rm min}$s simultaneously, we slightly change $R_{\rm mod}$ in some cases.

4.2 Properties of the MESA evolution code

The interior models are constructed using star and astero modules of the MESA (version 15140) stellar evolution code (Paxton et al. 2011, 2013, 2015, 2018, 2019; Jermyn et al. 2023). Based on the calibration of the solar model, the values of $Y_\odot$ $Z_\odot$, and convective parameter ($\alpha_\odot$) values are obtained as 0.2745, 0.0172, and 1.814, respectively.

The standard mixing length theory of Böhm-Vitense et al. (1958) is used for convection. The interior models do not consider convective overshooting. The opacity for high T values is determined from OPAL (Iglesias & Rogers 1993, 1996), while that for the low T values are taken from the tables in Ferguson et al. (2005). In addition, the Nuclear Astrophysics Compilation of Reaction Rates (NACRE) tables (Angulo et al. 1999) are used for nuclear reaction rates. We also test different rates for the ^{14}N(p,γ)^{15}O reaction. These rates are controlled with `set_rate_n14pg = 'jina reaclib'` and `set_rate_n14pg = 'NACRE'` in MESA (see Section 5). Element diffusion is applied using the method proposed by Paquette et al. (1986). Atmospheric conditions affect the adiabatic oscillation frequencies of the model. The option `simple_photosphere` in the MESA code is used for the stellar interior models. In this study, the pre-MS phase is included in the construction of the stellar interior models.

The adiabatic oscillation frequencies of the evolutionary model are calculated using the ADIPLS package (Christensen-Dalsgaard 2008). In interior models, the surface layers of the star cannot be modelled exactly. Therefore, the Kjeldsen et al. (2008) surface-effect correction is applied to the model frequencies.

To compare the mixed mode frequencies of models and those obtained from observations, we use the astero module of MESA. This module includes a list of observational frequencies in its input file. Near-surface effects are computed using the "combined" option of Ball & Gizon (2014).

4.3 Modelling method and uncertainty calculations

Input parameters needed to construct an interior model are M, initial helium abundance (Y_0), initial metallicity (Z_0) and α. In this work, we uses the masses M_π and $M_{\rm sca}$ as the initial mass (Section 4.1). Z is obtained either from colours or from the [Fe/H] value determined from the spectra, and α is taken as the solar value. The last remaining input parameter Y_0 is used to fit the model to the position of the star in the HR diagram. Y_0 is changed so that the model parameters fit the observational values of R and L. Model construction starts with $Y_0 = Y_\odot$. If the model is not in agreement with the observations, a new model is computed with new Y_0. This process is repeated until a model compatible with the observation point in Fig. 2 is obtained.

In the next step, model and observational seismic data (such as ν, $\langle\Delta\nu\rangle$ and $\nu_{\rm min}$s) are compared. Suppose there is no agreement within the uncertainty; a new mass value is calculated to fit the observational $\langle\Delta\nu\rangle$ using the scaling relation. This process is repeated with a new value of M and continues until an agreement is achieved within the uncertainty of $\langle\Delta\nu\rangle$. The outputs of the models calibrated in this way are listed in Table 3.

Further, we obtain unique models using the χ^2-method. According to the surface metallicity ($Z_{\rm s} \sim 0.01$) of the star determined from its spectra, the initial metallicity is approximately 0.012. We obtain very dense grids in all the important model input parameters (M, Z_0, Y_0, and α) at different ages (see Section 5.1.2). Then, we apply the normalised χ^2 - method for the asteroseismic constraints. This method gives very small values of χ^2, which are concentrated at a certain point in the multi-variable parameter space. This aspect is considered a unique feature of the interior model if there is a single point at which χ^2 is minimum in the multi-dimensional variable space.

Uncertainties in the values of M, R, $\log g$, L and t computed in this study are estimated by Monte-Carlo simulations. The method is repeated on each synthetic data set, and the standard deviation of the distribution after 1000 iterations is taken as an estimate of the

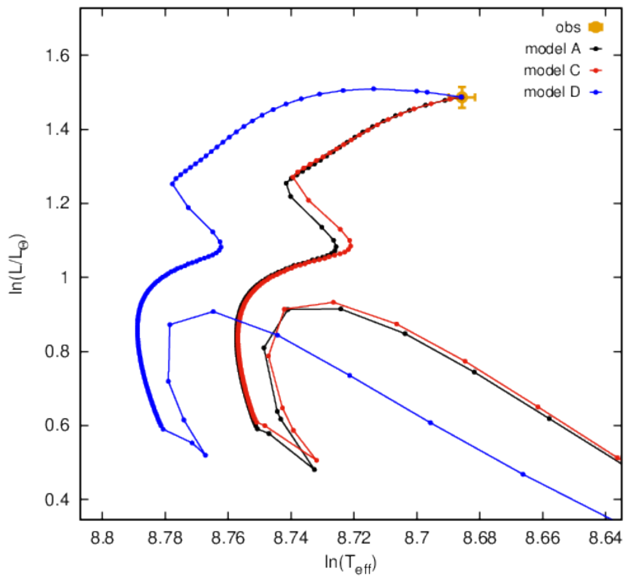

Figure 2. HR diagram. The diagram shows the evolutionary tracks of Models A, C and D. Although the models fit the same observation point, they have different evolutionary tracks. Models A, C and D are represented by solid circles in black, red and blue, respectively. The filled yellow circle indicates the observation point on the HR diagram for KIC 7747078.

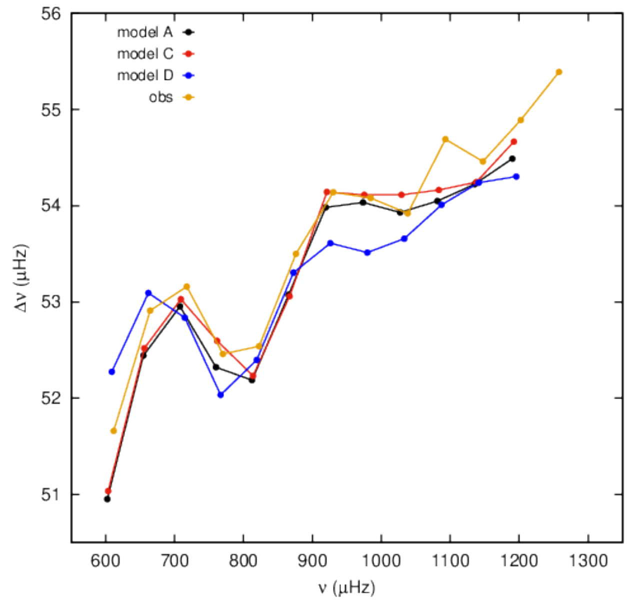

Figure 3. $\Delta\nu$ is plotted with respect to ν. The filled yellow circle indicates the observational frequencies of KIC 7747078. The filled black, red and blue circles represent the adiabatic oscillation frequencies of Models A, C and D, respectively.

uncertainty. The uncertainties in the outputs of the models are also listed in Table 3.

5 RESULTS AND DISCUSSIONS

The small separation is a strong age indicator for the solar-like oscillating stars. The value of $\delta\nu_{02}$ is maximum around the ZAMS, while it is approximately 5-6 μHz around the TAMS. In evolved stars, the sensitivity of the small separation to the core structure decreases as the internal structure of the star changes. Therefore, strong constraints and precise observational data are needed to construct a unique model for evolved stars. These observational data are used in the methods described in Section 4.1 to estimate the fundamental properties of the star, such as M and R.

The fact that the luminosity of KIC 7747078 is close to its maximum ($L_{\rm max}$) after TAMS is advantageous for modelling. Luminosity in the HR diagram ($L \approx L_{\rm max}$) remains almost constant with age as it is determined by M, Z_0, and Y_0. When multiple parameters are involved, the ineffectiveness of some parameters brings the solution closer to a unique solution. For such stars, for example, we can construct models whose α and age values differ while the remaining features are the same (see Models A and D in Table 3), and we can examine their asteroseismic properties.

5.1 Interior models with high Z

The $T_{\rm eff}$ and Z values can also be obtained from the $(B-V)$ and $(V-K)$ colours. Using the colour tables of Lejeune, Cuisinier & Buser (1998), we estimate $T_{\rm eff}$ to be about 6160 K and Z to be 0.0220. These values are significantly higher than those obtained from spectral analysis (see Table 1).

We first construct models fitted to the spectral and asteroseismic data in Tables 1 and 2, respectively. Table 3 lists the results of all the calibrated models with the JINA reaction rate (Cyburt et al. 2010) for ^{14}N(p,γ)^{15}O (`set_rate_n14pg = 'jina reaclib'`). Although the models fit the parameters (L, R, $T_{\rm eff}$, etc.) determined from the observational data, models may have different M, t, α, ν and $\nu_{\rm min}$s. Fig. 2 shows the evolutionary tracks of three models (Models A, C and D in Tables 3 and 4) with different M and α values. R and $T_{\rm eff}$ of these models are 2.00 R$_\odot$ and 5918 K, respectively. Despite the significant differences in their evolutionary tracks, the input parameters of models A and D are identical, except for their αs. Model A has $\alpha_\odot$ while the α value of model D is greater than $\alpha_\odot$: α = 2.454. The $T_{\rm eff}$ difference between models D and A is approximately 180 K during the MS phase but zero at the observed position of the star in the HR diagram. Since Model D is slightly more evolved than Model A, its age is slightly higher than that of Model A. Models A and D have the same mean density, and therefore, they must have identical $\Delta\nu$ values (Fig. 3). We need to know if there is any difference between the asteroseismic properties of these two models (see below).

Models A and C have equal α values and slightly different masses. Model C has a slightly higher mass, and its age is slightly less than that of Model A. Additionally, the Z_0 values of the two models differ by around 0.001. It is not easy to determine which of these three models, which intersect at the same point on the HR diagram, represents KIC 7747078. Asteroseismic analysis can reveal which of these models best represents the star.

5.1.1 *Distinguishing models with $\nu_{\rm min}$s and individual frequencies*

Although the model input parameters in Table 3 are very close to each other, it has sufficient coverage considering the possible Z_0 - Y_0 relationship and asteroseismic data. Since $\langle\Delta\nu\rangle$ and $\nu_{\rm max}$ are related to the general properties of the star (equations (1) and (2)), they are not very suitable for distinguishing between models. Models A and D, for example, have the same mass and radius, and therefore their

Table 3. Fundamental parameters of the models. The columns present the model name, mass (M), radius (R), effective temperature ($T_{\rm eff}$), metallicity (Z_0), helium abundance (Y_0), convective parameter (α), age (t_9), reference frequencies ($\nu_{\rm min0}$ and $\nu_{\rm min1}$), large separation ($\Delta\nu$), frequency of the maximum amplitude ($\nu_{\rm max}$) and the mean of the difference between the model and observed frequencies ($\overline{d\nu}$). The last row of the table lists the observed $\nu_{\rm min0}$ and $\nu_{\rm min1}$ values sourced from Yıldız et al. (2019) and $\Delta\nu$ and $\nu_{\rm max}$ sourced from Li et al. (2020a).

Model	M ($M_\odot$)	R ($R_\odot$)	$T_{\rm eff}$ (K)	Z_0	Y_0	α	t_9 (Gyr)	$\nu_{\rm min0}$ (μHz)	$\nu_{\rm min1}$ (μHz)	$\langle\Delta\nu\rangle$ (μHz)	$\nu_{\rm max}$ (μHz)	$\overline{d\nu}$ (μHz)
A	1.208	2.00	5918	0.0161	0.2702	1.814	5.24	1038.21	794.89	53.22	921.60	10.57
	±0.021	±0.01	±25	±0.0003	±0.0040	—	±1.06	±12.13	±9.29	±0.31	±19.32	—
B	1.308	2.07	5918	0.0200	0.2584	1.814	4.77	1068.24	802.60	52.57	931.54	21.02
	±0.022	±0.01	±25	±0.0003	±0.0040	—	±0.96	±12.54	±9.42	±0.31	±18.94	—
C	1.213	2.00	5918	0.0172	0.2763	1.814	5.11	1049.34	813.81	53.33	925.41	8.87
	±0.020	±0.01	±25	±0.0003	±0.0050	—	±1.02	±12.37	±9.59	±0.31	±19.23	—
D	1.208	2.00	5918	0.0161	0.2702	2.454	5.42	1004.01	783.07	53.27	921.60	4.16
	±0.021	±0.01	±25	±0.0003	±0.0040	—	±1.10	±8.28	±6.46	±0.22	±19.84	—
E	1.275	2.02	6160	0.0220	0.3060	2.454	4.04	1093.25	831.90	53.61	934.63	0.10
	±0.021	±0.01	—	±0.0004	±0.0050	—	±0.84	±10.93	±8.32	±0.27	±20.22	—
F	1.279	2.03	6094	0.0267	0.3200	2.454	4.02	1118.59	833.43	53.42	933.36	2.78
	±0.022	±0.01	—	±0.0005	±0.0050	—	±0.82	±11.23	±8.37	±0.27	±19.65	—-
obs	—	—	—	—	—	—	—	1039.3	792.5	53.22	931	—
	—	—	—	—	—	—	—	±10.4	±7.9	±0.01	±5	—

Table 4. Observed oscillation frequencies of the $l = 0$ mode, as reported in the literature for KIC 7747078, and frequencies of the six models constructed in this study.

Appourchaux et al. (2012)	Li et al. (2020a)	Model A	Model B	Model C	Model D	Model E	Model F
559.634±—–	559.83±0.101	551.311	544.715	552.393	556.462	559.099	557.222
612.376±1.272	611.49±1.256	602.264	595.138	603.429	608.738	611.027	609.097
664.495±0.201	664.40±0.307	654.707	646.486	655.948	661.831	663.703	661.649
717.500±0.124	717.56±0.109	707.661	698.887	708.977	714.667	717.466	715.232
769.836±0.183	770.02±0.065	759.983	751.102	761.573	766.703	770.674	768.350
822.395±0.181	822.56±0.058	812.171	802.596	813.806	819.100	823.078	820.574
876.056±0.124	876.06±0.054	865.246	854.825	866.866	872.405	876.145	873.333
929.999±0.099	930.20±0.054	919.229	907.920	921.009	926.015	930.188	927.110
984.210±0.108	984.28±0.064	973.263	961.439	975.123	979.528	984.633	981.307
1037.893±0.212	1038.20±0.262	1027.193	1014.949	1029.235	1033.187	1039.014	1035.492
1092.389±0.235	1092.89±0.256	1081.241	1068.240	1083.399	1087.195	1093.255	1089.554
1146.166±0.582	1147.35±0.624	1135.465	1121.881	1137.644	1141.435	1147.695	1143.719
1201.562±0.699	1202.24±1.209	1189.953	1175.592	1192.310	1195.738	1202.440	1198.250

$\Delta\nu$ and $\nu_{\rm max}$ are very close to each other. For such cases, we also compare the individual oscillation frequencies of models with the observed frequencies. Individual oscillation frequencies of the models depend on the input parameters and surface effect. The difference between the mean frequency of Model A and the observed frequencies ($\overline{d\nu} = \nu_{n0,\rm obs} - \nu_{n0,\rm mod}$) is approximately 11 μHz. This difference is very small compared to the individual frequencies and may be due to surface effects. Therefore, the use of individual oscillation frequencies alone may be insufficient to distinguish the models. In such cases, different asteroseismic parameters, such as reference frequencies, are needed to distinguish models because $\nu_{\rm min}$s of Models A and D are significantly different.

We investigate whether the models can be distinguished in terms of the reference frequencies introduced by Yıldız et al. (2014). These are the frequencies corresponding to the minima in the $\Delta\nu$-ν graph due to the glitches induced by the second helium ionization zone on the oscillation frequencies. These reference frequencies can be detected at the evolutionary stages MS, SG and RG. With evolution, the structure of the minima in the $\Delta\nu$-ν graph changes and shifts towards lower frequencies. $\nu_{\rm min1}$ is in general seen in the oscillation frequencies of all the solar-like oscillators. However, $\nu_{\rm min2}$ is available for the relatively hot oscillators, $\nu_{\rm min0}$ is more prominent in particular for the cooler oscillators. $\nu_{\rm min1}$ and $\nu_{\rm min0}$ of KIC 7747078 are shown in Fig. 4.

To find any $\nu_{\rm min}$, we first determine the frequency interval of a certain minimum in the graph of $\Delta\nu$ versus ν. Two lines are drawn for the neighbourhood intervals. The intersection of the two lines gives the reference frequency $\nu_{\rm min}$. The method to determine $\nu_{\rm min}$ is shown in Fig. 4. The value of $\nu_{\rm min}$ depends on the fundamental parameters of the star, such as M, R and $T_{\rm eff}$. In the $\Delta\nu - \nu$ graph of KIC 7747078, the reference frequencies $\nu_{\rm min1}$ and $\nu_{\rm min0}$ correspond

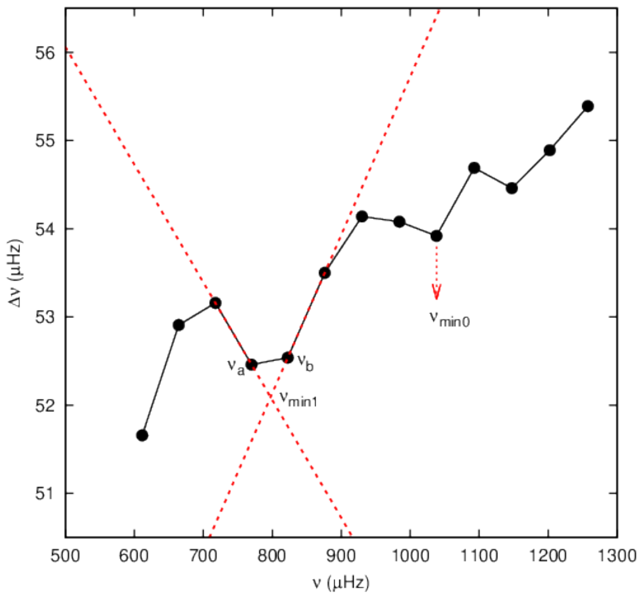

Figure 4. Graph of $\Delta\nu$ versus ν for determining the reference frequencies $\nu_{\rm min1}$ **and** $\nu_{\rm min0}$. The reference frequency $\nu_{\rm min1}$ is between $\nu_{\rm a}$ and $\nu_{\rm b}$. We plot two lines from the neighbourhood intervals. The intersection of these two lines gives us $\nu_{\rm min1}$. $\nu_{\rm min0}$ is around an observed frequency. The $\nu_{\rm min1}$ and $\nu_{\rm min0}$ values of the star are found to be 792.5 and 1039.3 μHz, respectively.

to the minima at low and high frequencies, i.e. 792.5 and 1039.3 μHz, respectively.

When determining $\nu_{\rm min0}$, particular care is needed owing to the shallowness of the trough, which can make the determination of observational $\nu_{\rm min0}$ challenging (Fig. 4). Therefore, it is necessary to track how the minima change with evolution using grids. For KIC 7747078, an evolved star, mixed modes obscure clear minima in the $\Delta\nu$ - ν plot for modes with $l > 0$. Therefore, we use reference frequencies from modes with $l = 0$ to find the best model. In addition to these asteroseismic parameters, we use individual oscillation frequencies as constraints for interior models. In this case, we use the parameters of the best model obtained using Kjeldsen et al. (2008) method for the near-surface effects as the initial parameter and construct a new model (Model AN in Table 5) using astero modules with the "combined" option (Ball & Gizon 2014). This model effectively fulfills all observational constraints, including mixed mode frequencies (Section 5.4).

Asteroseismic methods generally provide more accurate results for $\log g$ compared to spectroscopic methods (Chaplin & Miglio 2013). Therefore, asteroseismic $\log g$ is used as a benchmark when selecting spectral data. The spectral $\log g$ reported by Bruntt et al. (2012) is in good agreement with the seismic $\log g$ given by Yıldız et al. (2019) and Li et al. (2020a) ($\log g_{\rm seis}$ = 3.91). $T_{\rm eff}$ is 5840 K, as determined by Bruntt et al. (2012) from spectral analysis. First, this value of $T_{\rm eff}$ is used as one of the constraints for the interior models of KIC 7747078. However, for this value, neither the individual oscillation frequencies nor $\nu_{\rm min}$ values agree with the observational values.

The $\log g$ value reported by Brewer et al. (2016) is close to the $\log g_{\rm seis}$ value. The researchers reported $T_{\rm eff}$ to be 5918 K. The $\nu_{\rm min1}$ and $\nu_{\rm min0}$ values of the model constructed under constraints of this spectral data are 794.89 and 1038.21 μHz, respectively. They are in close agreement with the observed $\nu_{\rm min}$ values (Model A in Table

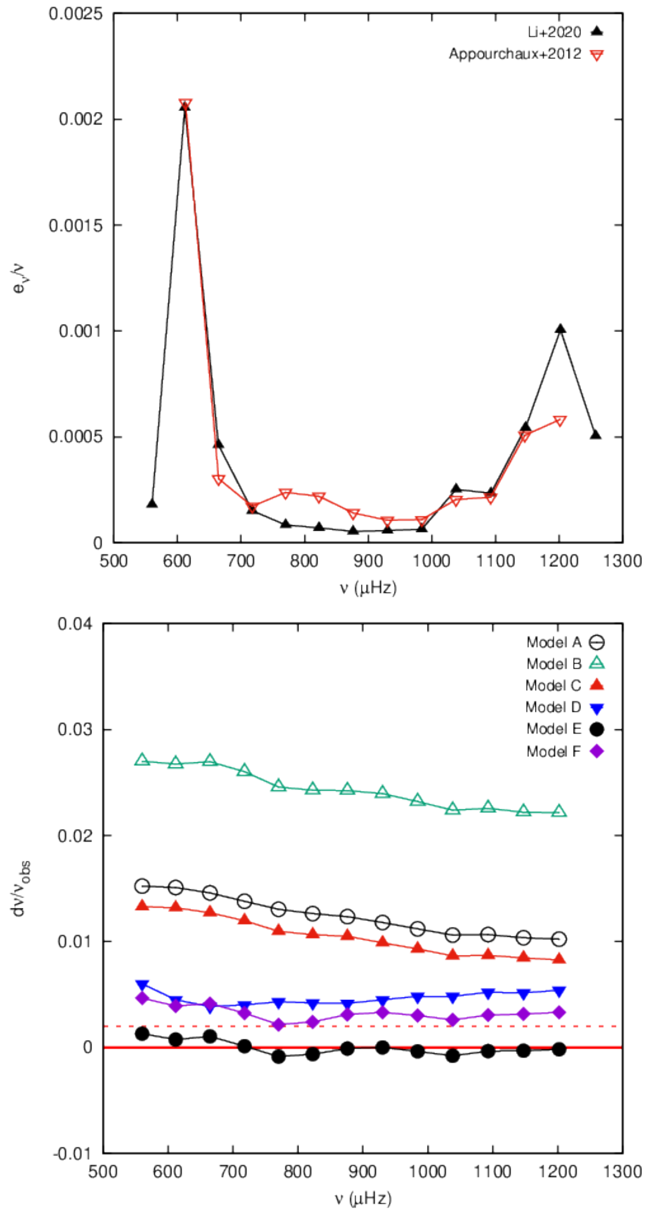

Figure 5. The upper panel shows the uncertainty (e_ν) of the observation frequencies of KIC 7727078 that is plotted with respect to $\nu_{\rm obs}$. The filled black triangles and the hollow red triangles represent the frequencies as reported by Li et al. (2020a) and Appourchaux et al. (2012), respectively. The lower panel plots the fractional difference between the observational and model frequencies with respect to $\nu_{\rm obs}$. The graph shows the results obtained by six models. Model E provides the best agreement with the observational frequencies.

3). However, there exists a mean difference of 11 μHz between the observational and model individual frequencies.

We can try to eliminate this difference. To increase the model frequencies by 11 μHz, we keep R constant and estimate M = 1.213 $M_\odot$ from the basic relationship between the stellar mean density and oscillation frequency of a certain mode. A model with this mass (Model C) has $\langle\Delta\nu\rangle$ =53.33 μHz; however, this value should be around 53.67 μHz according to the asymptotic relation. This discrepancy reveals that the asymptotic relation works slightly differently than our ex-

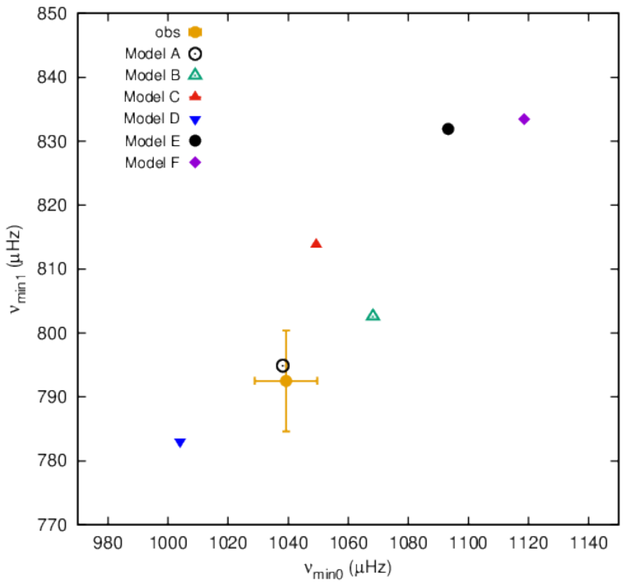

Figure 6. The plot of $\nu_{\rm min0}$ against $\nu_{\rm min1}$. The graph shows the reference frequencies of the six models. The solid yellow circle with error bars represents the observational reference frequencies. The observational values of $\nu_{\rm min1}$ and $\nu_{\rm min0}$ are 792.5 and 1039.3 μHz, respectively. Model A gives a common solution for $\nu_{\rm min1}$ and $\nu_{\rm min0}$.

pectation. Although these values are very close, the difference is considerable if we compare the model results with the observational values of Li et al. (2020a). When we compare Models C and A, we see that although the individual frequencies are improved slightly, the difference between the observational and model reference frequencies increases.

In Model A, both minima are in very good agreement with the observational data. However, there is a difference of 11 μHz between the observational and model oscillation frequencies. To eliminate this difference, the convective mixing length parameter α is changed. In Model D, the input parameters M, Z_0 and Y_0 are taken as the same as those in Model A. Only the parameter α is taken as 2.454 instead of $\alpha_\odot$. Fig. 2 shows the evolutionary tracks of Model A (filled black circle) and Model D (filled blue circle). Increasing α increases the effective temperature of the star, and the evolutionary track of the star shifts to the left in the HR diagram. The effect of α on the individual oscillation frequencies needs to be determined. The mean difference between the model and observational individual frequencies decreases to 4 μHz. The good agreement obtained for $\nu_{\rm min1}$ and $\nu_{\rm min0}$ in Model A is not achieved in Model D. The difference between observational and model $\nu_{\rm min1}$ becomes 10 μHz. The difference for $\nu_{\rm min0}$ is 30 μHz.

The $\nu_{\rm max}$ values of Models A and C are 6 − 9 μHz less than the observed $\nu_{\rm max}$ value (Li et al. 2020a). To realise the agreement between the observed and model $\nu_{\rm max}$, we construct Model B with 1.308 M$_\odot$ and 2.07 R$_\odot$. The $\langle\Delta\nu\rangle$ of Model B is 52.57 μHz, which is less than the observed value. The mean difference between the observed and Model B frequencies is approximately 21 μHz. This is the greatest difference in $\overline{d\nu}$ among the whole interior models listed in Table 3. This implies that it is not easy to achieve the simultaneous fit of $\langle\Delta\nu\rangle$, νs and $\nu_{\rm max}$ of a model to the observed values. This result probably indicates that we need to improve the scaling relation for $\nu_{\rm max}$. However, $\nu_{\rm min1}$ and $\nu_{\rm min0}$ of Model B shift towards higher frequency values, reaching 802.60 and 1068.24 μHz, respectively.

5.1.2 Effect of $T_{\rm eff}$ on individual frequencies

Using the α value of Model D, we construct a new model with $T_{\rm eff}$ = 6160 K and Z = 0.0220. This model is labelled as Model E in Table 3. Its $\overline{d\nu}$ has the smallest value (0.1 μHz) among the models. If we consider only the individual oscillation frequencies, Model E is the best model for KIC 7747078. However, $\nu_{\rm min1}$ and $\nu_{\rm min0}$ of Model E are significantly greater than the observed values. The difference between the model and observed values of $\nu_{\rm min}$s is about $\langle\Delta\nu\rangle$.

We construct Model F with slightly modified parameters of Model E. Its $T_{\rm eff}$ and Z_0 are 6094 K and 0.0267, respectively. Both the reference and the individual frequencies of Model F are greater than those of Model E.

Table 4 lists the observational and model frequencies for l = 0. The first two columns are the observational frequencies given in the literature. The mean difference between the observational individual oscillation frequencies and that of Model E is approximately 0.1 μHz. The top panel of Fig. 5 shows the uncertainty of the oscillation frequencies (e_ν) given in Appourchaux et al. (2012) and Li et al. (2020a). The uncertainty is large around ν = 600 μHz. If this datum is ignored, the fractional uncertainty ($\overline{d\nu}/\nu$) decreases to 0.001. Model frequencies are also analysed by considering these observational frequencies. The bottom panel of Fig. 5 shows the fractional difference between Li et al. (2020a) and model frequencies. The dashed red line represents the upper limit of the uncertainty. Accordingly, Model B has the highest difference, while Model E is below the dashed line, giving a distribution around 0.

Fig. 6 shows the reference frequencies plotted against each other. The observational position of KIC 7747078 ($\nu_{\rm min1}$ = 792.5 μHz and $\nu_{\rm min0}$ = 1039.3 μHz) is plotted along with error bars. The model closest to the observed position of the star in Fig. 6 is Model A.

The $\langle\Delta\nu\rangle$ of all models (Table 3) are compatible with the observational $\langle\Delta\nu\rangle$. The $\nu_{\rm min1}$ and $\nu_{\rm min0}$ of Model A agree very well with the observational $\nu_{\rm min1}$ and $\nu_{\rm min0}$, while the individual observational frequencies of Model E agree very well with the observational frequencies. The reference frequencies of Model E exceed the observational values by approximately $\langle\Delta\nu\rangle$ (54 and 39 μHz). The difference between Model A and observational individual frequencies is 11 μHz. If we consider only the asteroseismic data, Model A is much more consistent with observations because its $\overline{d\nu} << \langle\Delta\nu\rangle$. The difference between individual frequencies is related to the surface effect. However, the shortcoming of Model A is its $Z_{\rm s}$ = 0.0139 ([Fe/H] = +0.016) which is significantly greater than the observed values listed in Table 1.

The asteroseismic $\langle\Delta\nu\rangle$ parameter can be determined from the power spectrum. The most sensitive value for KIC 7747078 is 53.22 μHz reported by Li et al. In cases where individual frequencies are determined observationally, we can calculate $\langle\Delta\nu\rangle$ as the mean difference between the frequencies of successive modes. The $\langle\Delta\nu\rangle$ value we calculated for this star is 53.4 μHz. Another important aspect regarding sensitive models under asteroseismic constraints is selecting the value of $\langle\Delta\nu\rangle$. Since we calculated the $\langle\Delta\nu\rangle$ of the model from the differences between frequencies, it is more appropriate to use the $\langle\Delta\nu\rangle$ calculated similarly (53.4 μHz). In the following section, we use both values of $\langle\Delta\nu\rangle$ as constraints for the interior models.

5.2 Effect of metallicity and χ^2-method for modelling

Literature reports large differences in the parameter values, espe-

Table 5. Basic properties of the models constructed using the χ^2- method. The columns are ordered as follows: model name, mass (M), radius (R), effective temperature ($T_{\rm eff}$), initial metallicity (Z_0), initial helium abundance (Y_0), convective parameter (α), age (t_9), reference frequencies ($\nu_{\rm min0}$ and $\nu_{\rm min1}$), large separation ($\Delta\nu$), frequency of maximum amplitude ($\nu_{\rm max}$), surface metallicity (Z_s), $\chi^2_{\rm seis}$, mixture of metallicity for low-opacity temperature (Asplund et al. 2009; Grevesse & Sauval 1998) and module. Models N1 − N7 are derived using the NACRE reaction rate for ^{14}N(p,γ)^{15}O. Model J is obtained with the JINA rate for that reaction. Model AN in the last row is constructed using the astero module. The constraint for $\langle\Delta\nu\rangle$ is 53.4 μHz for Models N1 − N4, and 53.22 μHz for Models N5 − N7 and J. Our favourite models are N1 and N6 with 53.4 and 53.22 μHz, respectively. The basic parameters of the models are quite similar, implying that our method provides a unique model for KIC 7747078.

Model	M (M$_\odot$)	R (R$_\odot$)	$T_{\rm eff}$ (K)	Z_0	Y_0	α	t (Gyr)	$\nu_{\rm min0}$ (μHz)	$\nu_{\rm min1}$ (μHz)	$\Delta\nu$ (μHz)	$\nu_{\rm max}$ (μHz)	Z_s	$\chi^2_{\rm seis}$	mixture	module
N1	1.17	1.975	5977	0.0121	0.2689	1.8311	5.17	1037.4	791.2	53.40	910.76	0.0103	0.02	gs98	star
N2	1.17	1.975	5993	0.0120	0.2711	1.8311	5.08	1046.3	794.7	53.40	909.82	0.0102	0.18	gs98	star
N3	1.17	1.975	5996	0.0120	0.2711	1.8511	5.09	1050.7	792.6	53.40	909.71	0.0103	0.40	gs98	star
N4	1.17	1.970	6048	0.0120	0.2711	1.8311	5.06	1040.6	799.1	53.51	909.78	0.0097	0.34	a09	star
N5	1.17	1.979	5988	0.0120	0.2711	1.8311	5.08	1032.1	790.4	53.22	905.97	0.0102	0.18	gs98	star
N6	1.18	1.985	6005	0.0120	0.2687	1.8311	5.00	1039.4	796.2	53.22	907.47	0.0102	0.07	gs98	star
N7	1.17	1.979	5990	0.0120	0.2711	1.8511	5.09	1033.4	788.7	53.22	905.85	0.0103	0.18	gs98	star
J	1.16	1.973	6011	0.0120	0.2711	1.8511	5.26	1043.0	789.1	53.21	901.94	0.0100	0.10	gs98	star
AN	1.17	1.961	5993	0.0121	0.2689	1.8311	5.15	1037.8	809.4	53.55	927.04	0.0103	0.34	gs98	astero

cially, $T_{\rm eff}$, determined from the spectral data. In the above models, while the $T_{\rm eff}$ values of the models are compatible with the observation, there is a significant difference between $Z_{\rm s}$. According to the observational [Fe/H] values given in Table 1, $Z_{\rm s}$ ranges from 0.0074 to 0.0104. These values are significantly lower than those of the models in Table 3 ($Z_{\rm s}$ = 0.013 − 0.025). Hence, we aim to construct a more suitable model.

Recently, many studies have explored the rate of the ^{14}N(p,γ)^{15}O nuclear reaction. For the rate of this reaction, MESA has NACRE (`set_rate_n14pg = 'NACRE'`) and JINA options. Previous models are constructed using JINA. Models constructed with the NACRE option are listed in Table 5. In NACRE (Angulo et al. 1999) and JINA (Cyburt et al. 2010), the S-factor for this nuclear reaction was taken as 1.77 ± 0.20 (Angulo & Descouvemont (2001)) and 1.61 ± 0.08 (Imbriani et al. 2005), respectively.

Table 5 also lists the surface chemical compositions and $\chi^2_{\rm seis}$ values of the models obtained with JINA and NACRE reaction rates for ^{14}N(p,γ)^{15}O. The $\chi^2_{\rm seis}$ of the models are computed from

$$\chi^2_{\rm seis} = \frac{1}{3}\sum_{i=1}^{3}\left(\frac{f_{i\rm obs} - f_{i\rm mod}}{e_{i\rm obs}}\right)^2 \quad (7)$$

where $f_{i\rm obs}$ are the observed values of $\langle\Delta\nu\rangle$, $\nu_{\rm min0}$ and $\nu_{\rm min1}$. Their uncertainties and model values are represented by $e_{i\rm obs}$ and $f_{i\rm mod}$, respectively.

When constructing the interior models listed in Table 5, we do not calibrate the models over M, R or $T_{\rm eff}$. We only consider the asteroseismic parameters in the computation of $\chi^2_{\rm seis}$ and check if the models with sufficiently small χ^2 value have $Z_{\rm s}$ in good agreement with the observations. As a result of the analysis, M, R and $T_{\rm eff}$ are given as output. In conclusion, three asteroseismic and one spectroscopic ($Z_{\rm s}$) constraints can be used to build a unique interior model for KIC 7747078.

These models are those with the smallest $\chi^2_{\rm seis}$ values among many constructed using Z_0 = 0.0115 − 0.0125, M = 1.15 − 1.20, α = 1.8111 − 1.8511, Y_0 = 0.2687 − 0.2723 and t_9 = 4.6 − 6.0. The first four rows of Table 5 show the $\chi^2_{\rm seis}$ of the models computed by taking $\langle\Delta\nu\rangle$ = 53.40μHz. The smallest $\chi^2_{\rm seis}$ value is for Model N1 obtained using M = 1.17 M$_\odot$, R = 1.975 R$_\odot$, Z_0 = 0.0121, Y_0 = 0.2689, and α = 1.8311. The age of this model is 5.17 Gyr. For this model, $Z_{\rm s}$ = 0.0103, which is in good agreement with the observational values. This is our favourite model with the NACRE rate for ^{14}N(p,γ)^{15}O. For Model N2, where only Y_0 is slightly higher and the remaining parameters are the same, $\chi^2_{\rm seis}$ = 0.18. The value of $\chi^2_{\rm seis}$ for the next model (Model N3) is 0.40. This value is obtained with a slightly greater value of α (α = 1.8511) compared to that of Model N2.

The $Z_{\rm s}$ of models listed in Table 5 is approximately 0.01. This value implies that [Fe/H] = −0.127, which agrees better with the observed values given in Table 1 than the value of Model A in Table 3. The $Z_{\rm s}$ of Model N4 corresponds to [Fe/H] = −0.140, which is in perfect agreement with the observed value of [Fe/H] reported by Brewer et al. (2016). The difference between Model N4 and Models N1 - N3 is the mixture of metallicity for the low-opacity temperature. For Model N4, the mixture is as reported by Asplund et al. (2009) (`kap_lowT_prefix = 'lowT_fa05_a09p'`). The remaining models contain the mixture reported by Grevesse & Sauval (1998) (GS98, `kap_lowT_prefix = 'lowT_fa05_gs98'`). Models N2 and N4 have identical M, Z_0, Y_0 and α values. The $Z_{\rm s}$ of Model N4 is slightly less than that of Model N2. The $\chi^2_{\rm seis}$ value increases to 0.34 for Model N4.

Models N5 – N7 are constructed using $\langle\Delta\nu\rangle$ = 53.22 μHz. Among them, Model N6 shows the lowest $\chi^2_{\rm seis}$. This model is very similar to Model N1, and the mass difference between them is 0.01 M$_\odot$. Models 5 and 7 have identical input parameters (M, Y_0 and Z_0) except α, and they provide similar model results, including the ages.

Model J, detailed in Table 5, is constructed with the `set_rate_n14pg = 'jina reaclib'` option for ^{14}N(p,γ)^{15}O, for which M = 1.160 M$_\odot$ gives the smallest value of $\chi^2_{\rm seis}$ as 0.10.

The effects of different input parameters, such as mixtures of metallicity and nuclear reaction rate options, on frequencies have been tested. The models analysed are listed in Table 5. Although the models are similar, the values of $\nu_{\rm min0}$ and $\nu_{\rm min1}$ vary between 1030 − 1050 μHz and 788 − 800 μHz, respectively, causing differ-

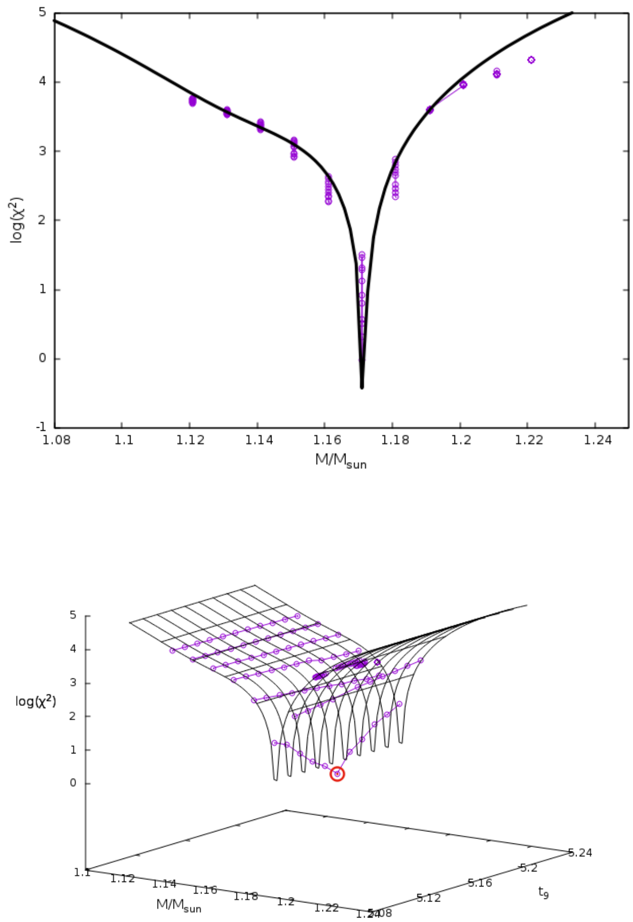

Figure 7. In the upper panel, logarithmic $\chi 2$ is plotted against mass using the grid for KIC 7747078. Z_0 of the models is 0.0121. The lowest χ^2 value is achieved at a mass of 1.171 $\mathrm{M}_\odot$. In the lower panel, logarithmic $\chi 2$ is plotted against M and t_9. M and t_9 of the best model are 1.171 $\mathrm{M}_\odot$ and 5.165 Gyr, respectively. t_9 does not distinguish models at other masses. The best model is highlighted using a red circle.

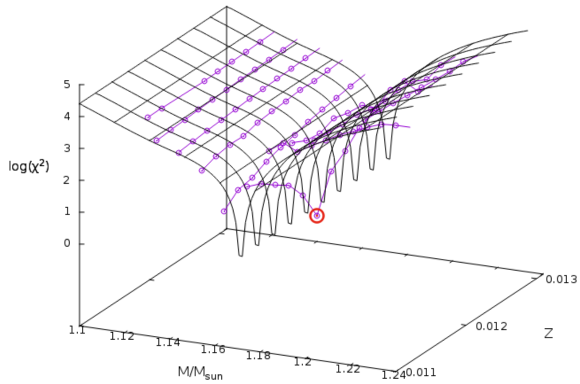

Figure 8. Logarithmic $\chi 2$ is plotted against M and Z_0, showing the smallest $\chi 2$ value at a certain M and Z_0, indicating the unique model at that M. M and Z_0 of the model are 1.171 $\mathrm{M}_\odot$ and 0.0121, respectively. Z_0 does not indicate another unique model in models with masses greater and less than 1.171 $\mathrm{M}_\odot$. The best model, as indicated by Z_0, is marked with a red circle.

ences in $\chi^2_{\rm seis}$. These changes in minima indicate how precise the method is.

5.3 Evolution grids for KIC 774708 and three-dimensional analysis

To verify the uniqueness of a model for KIC 7747078, we construct an evolution grid with varying M, Z_0 and age parameters. The grid ranges are 1.120-1.220 $\mathrm{M}_\odot$ for M, 0.0111-0.0131 for Z_0 and 5.12-5.22 Gyr for t_9. The grid steps are $\Delta M = 0.01\mathrm{M}_\odot$, $\Delta Z = 0.0002$ and $\Delta t_9 = 0.01$Gyr.

Accurate mass determination is crucial for identifying the best model, as indicated by a very low $\chi 2$ for a single value of M. The values $\nu_{\rm min1}$, $\nu_{\rm min0}$, $\Delta\nu$ and $Z_{\rm s}$ values are used to calculate $\chi 2$ for the grids. In the upper panel of Fig. 7, log $\chi 2$ is plotted versus mass. The Z value of the models in the upper panel is 0.0121. The lowest $\chi 2$ occurs at 1.171 $\mathrm{M}_\odot$, while masses other than this result in $\chi 2$ values exceeding 100. This result underscores the significance of accurate mass determination is reaching a unique model. In the lower panel of Fig. 7, log $\chi 2$ is plotted against M and t_9. Models with the lowest $\chi 2$ values, particularly at $M = 1.171 M_\odot$, are differentiated by t_9, though no t_9 distinction is observed in other masses. At 5.165 Gyr, $\chi 2$ is approximately 0.3. The best model we obtain with M and t_9 is marked with a red circle in the graph.

The second key parameter in stellar structure and evolution is Z. However, it is difficult to determine Z observationally. Asteroseismic modelling method can be used to estimate Z values. This study examines how Z_0 affects frequencies using the grid. In Fig. 8, log $\chi 2$ is plotted against M and Z_0, revealing a single solution where $\chi 2$ is minimised using asteroseismic parameters. The lowest $\chi 2$ value is achieved at $Z_0 = 0.0121$ for models with masses of 1.171 $\mathrm{M}_\odot$. Other Z_0 values do not yield a specific model for above or below 1.171 $\mathrm{M}_\odot$. The best model is drawn with a red circle in Fig. 8.

Using the grids, we derive several models with different fundamental parameters for KIC7747078. Upon examining the asteroseismic data, a unique model, referred to as Model N1, is identified. In this case, the M, Z_0 and t_9 values of the unique model with the lowest $\chi 2$ are 1.171 $\mathrm{M}_\odot$, 0.0121 and 5.165 Gyr, respectively.

5.4 Analysing mixed and radial modes of KIC 7747078 using the astero module of MESA

As stars evolve, some oscillation modes are mixed, with the mixed mode frequencies providing insights into the core structure of stars (Deheuvels et al. 2012; Beck et al. 2012). These frequencies exhibit p-mode features in the envelope and g-mode features in the core. Since there is no $l = 0$ mode in the g-mode, radial mode frequencies remain unaffected. Analysis of the observational $l = 1$ and $l = 2$ mode frequencies of the subgiant KIC 7747078 that $l = 1$ modes are strongly affected, while $l = 2$ modes are either unaffected or minimally affected.

The fractional difference of the $l = 1$ mode frequencies of model A and N1, which are good in terms of minima, and model E, which is good in terms of frequencies, with the observation is given in Fig. 9. Model N1 aligns with observational frequencies within a 0.01

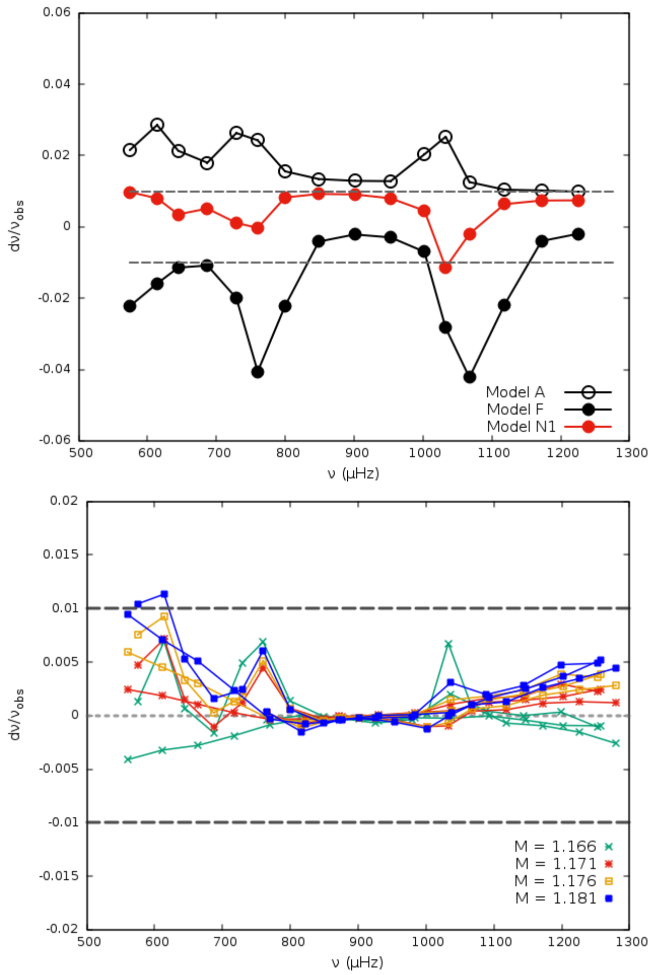

Figure 9. The fractional difference ($d\nu/\nu_{\rm obs}$) of the frequencies of the three models for the mode l = 1 is plotted against ν in the top panel. The dashed lines show the fractional difference of 0.01. Among the three models, N1 is the model that best matches the observation. In the bottom panel, fractional differences of the models constructed with the astero module for the modes l = 0, 1 and 2 are given. The most compatible models have a mass of 1.166 and 1.171 M$_\odot$.

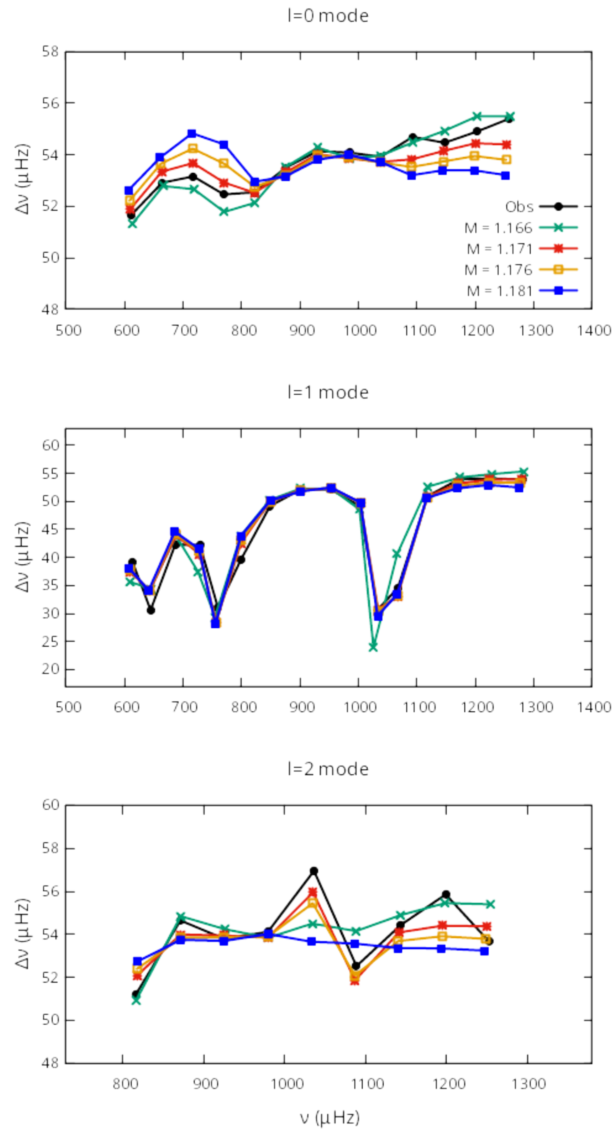

Figure 10. $\Delta\nu$ against ν plots for modes l = 0, 1 and 2 of models constructed using the astero module. The top panel shows the l = 0 mode, the middle panel the l = 1 mode and the bottom panel the l = 2 mode. While the model frequencies can be distinguished in modes l = 0 and l = 2, the models cannot be distinguished from each other in the l = 1 mode. The 1.166 and 1.171 M$_\odot$ models in the l = 0 mode and the 1.171 and 1.176 M$_\odot$ models in the l = 2 mode align well with the observational frequencies. The $\chi 2_{\rm seis}$ value calculated from $\nu_{\rm min1}$, $\nu_{\rm min0}$ and $\Delta\nu$ determined from the l = 0 mode indicates the model with a mass of 1.171 M$_\odot$ as the unique model.

fractional difference, whereas Models A and E exhibit differences up to 0.04. Among these three models, Model N1 best matches the mixed modes.

Using the parameters of the unique model N1, a new model is developed using the astero module of MESA. The results of the best model obtained from this module are presented as Model AN in the last row of Table 5. For this purpose, four models with Z_s =0.0100 were constructed in the range of 1.166 – 1.181 M$_\odot$, with increments of 0.005 M$_\odot$. These models are run until the radius provides the best match for the mode frequencies with l = 0, 1 and 2. The frequency values from all four models are aligned well with observations. The fractional difference between the model and the observed individual frequencies varies between -0.4 to 1.1 percent. The fractional differences for these astero models are shown in the bottom panel of Fig. 9. All models agree well with the observations at frequencies between 800 and 1000 μHz for modes l = 0, 1 and 2. However, the differences increase at frequencies above 1000 μHz and below 800 μHz. When the individual frequencies of the modes l = 0, 1 and 2 are examined together, the models with a mass of M = 1.166 M$_\odot$ and M = 1.171 M$_\odot$ give the lowest mean fractional difference.

The mixed mode frequencies with l = 1 align well with observational frequencies in the $\Delta\nu - \nu$ plot (middle panel in Fig. 10). For the l = 2 mode, two models, namely those with masses 1.171 M$_\odot$ and 1.176 M$_\odot$, fit zigzag structure seen in the $\Delta\nu - \nu$ plot (bottom panel in Fig. 10). This zigzag pattern at high frequencies becomes more linear at both lower and higher masses. Distinct patterns are observed for the l = 0 modes (top panel in Fig. 10), where the successive difference between frequencies increases at frequencies below approximately 900 μHz and decreases above it as mass increases.

The $\chi 2_{\rm seis}$ values, calculated using $\Delta\nu$, $\nu_{\rm min1}$ and $\nu_{\rm min0}$, are 0.83 and 0.34 for the 1.166 $M_\odot$ and 1.171 $M_\odot$ models, respectively. The other two models have $\chi 2_{\rm seis}$ values greater than 2. The unique model is Model AN (last row of Table 5) with a mass of 1.171 $M_\odot$, which has the lowest $\chi 2_{\rm seis}$ value of the four models.

The uncertainties in M, R and age are computed using the Monte Carlo simulation method and are found as 0.019 $M_\odot$, 0.011 $R_\odot$ and 0.28 Gyr, respectively.

Models N1 and AN exhibit very similar parameters, with the same M and Z_0. The differences in $T_{\rm eff}$, Y_0 and age are minimal. However, Model AN is identified as the best and unique model when individual frequencies are considered.

6 CONCLUSIONS

In this study, we analyze the SG star KIC 7747078, which was observed by the Kepler space telescope. The aim is to obtain a unique interior model representing the star using $\nu_{\rm min}$s and individual frequencies. We use $\nu_{\rm min}$ because the asteroseismic parameters such as $\Delta\nu$ and $\nu_{\rm max}$ are related to the general properties of the star (e.g. ρ and $\log g$). Therefore, stars with different masses and radii can have similar $\Delta\nu$ and $\nu_{\rm max}$. $\delta\nu_{02}$ is not a good indicator of the age of post-MS stars because a change in the internal structure of an evolved star reduces the sensitivity of this parameter to the core region. Hence, asteroseismic parameters such as $\Delta\nu$, $\nu_{\rm max}$ and $\delta\nu_{02}$ cannot be used to distinguish models for evolved stars.

The first step of the study is to estimate the mass and radius of the star using different methods (Section 4.1). The discrepancy among the previously reported data of the star makes it difficult to determine its fundamental parameters. This discrepancy also makes it difficult to construct a unique model of the star.

The interior models are constructed with the star and astero modules in the MESA evolution code. In our search for a unique model with a vast parameter pool, we mainly use the star module, which applies the standard Kjeldsen et al. (2008) correction for near-surface effects on oscillation frequencies. Once we obtain a unique model, we construct new models in the astero package by taking the parameters of this model as initial values and using the individual oscillation frequencies, and again obtain a unique model. In this module, we use the Ball & Gizon (2014) method to account for near-surface effects. The differences between the unique models obtained with the two modules are minimal.

For the interior models constructed using the star module, the initial model values are first calculated based on scaling relations. Each model shows a unique evolutionary track and age (see Fig. 2). To distinguish them, the frequency pattern is first examined. Since the frequencies of the models are intertwined in the $\Delta\nu - \nu$ graph, the models cannot be distinguished in this way. Therefore, the minimum and individual frequencies of the models are compared with observational values. Model A is obtained as the common solution as given per the $\nu_{\rm min1}$ and $\nu_{\rm min0}$ values of the models we constructed with $\alpha_\odot$. The difference between the frequencies of Model A and the observational frequency is 11 μHz, and the difference between the individual frequencies decreases with increasing α (Model D).

Two solutions are obtained using$(B-V)$ and $(V-K)$ colours and by comparing M_π and $M_{\rm sca}$. Models E and F show the results obtained using these solutions. Model E provides the best agreement with observational frequencies. However, the minima shift to higher frequencies.

Among the six interior models of KIC 7747078 given in Table 3, the reference frequencies of Model A and the individual frequencies of Model E are in very good agreement with the observations. The basic properties of Model A are $M = 1.208$ $M_\odot$, $R = 2.00$ $R_\odot$ and age $t = 5.24$ Gyr. For Model E, $M = 1.279$ $M_\odot$, $R = 2.02$ $R_\odot$ and $t = 4.04$ Gyr. These ages are significantly less than those reported by Chaplin et al. (2014) and in good agreement with the ages found by Yıldız et al. (2019).

While the $\nu_{\rm min0}$ and $\nu_{\rm min1}$ of Model A are in very agreement with the observations, the observational and model oscillation frequencies differ by 11 μHz. For Model D, which has a greater value of α ($\alpha = 2.454$) than Model A, the difference in frequencies reduces to about 4 μHz. However, the surface metallicity of these models does not agree with the observed spectral data.

We apply the χ^2-method to adopt the asteroseismic constraints. The three constraints of the models are the observed values of $\langle\Delta\nu\rangle$, $\nu_{\rm min0}$ and $\nu_{\rm min1}$. According to the $\chi^2_{\rm seis}$ value, for $\langle\Delta\nu\rangle = 53.4$ μHz, the best fitting model is Model N1 with $\chi^2_{\rm seis} = 0.02$. The basic parameters of Model N1 are as follows: $M = 1.17$ $M_\odot$, $R = 1.975$ $R_\odot$, $T_{\rm eff} = 5977$ K and $t_9 = 5.17$ Gyr. All the models listed in Table 3 with slightly different input parameters (M, R, Y_0 and α) are somewhat similar to Model N1. That is, the use of the three asteroseismic parameters and surface metallicity as constraints yields a unique interior model for KIC 7747078.

We demonstrate that it is feasible to identify a unique model of an evolved star using $\nu_{\rm min1}$, $\nu_{\rm min0}$, $\Delta\nu$ and Z_s. However, the mass needs to be obtained precisely. This is evident in the grids for KIC 7747078, where the minimum χ^2 value is observed at $M = 1.17$ $M_\odot$ for all combinations of M, Z_0 and t_9. The unique model with mass 1.171$M_\odot$ in the grid is strongly pointed with $Z_0 = 0.0121$ and $t_9 = 5.165$ Gyr.

In discussing a subgiant star's unique model, we examined the mode frequencies for $l = 0$, 1 and 2 (Fig. 10). For this, we construct interior models using astero module of MESA with initial parameters the same as that of Model N1. This module attempts to fit the model frequencies to the observed frequencies. In models with different masses, changes in $\nu_{\rm min1}$ and $\nu_{\rm min0}$ determined from $l = 0$ frequencies and different patterns in the $\Delta\nu - \nu$ graph led us to a single solution. However, the mixed modes with $l = 1$ appear unaffected by mass changes, while $l = 2$ frequencies show some mass-dependent variation, albeit less pronounced than $l = 0$. Therefore, $l = 0$ mode frequencies are found to be more effective in identifying a unique model. Among the four models, the model with $M = 1.171 \pm 0.019$ $M_\odot$ (Model AN) shows the lowest χ^2. Its age and initial helium abundance are 5.15 ± 0.29 Gyr and 0.2689, respectively. This is the unique model of KIC 7747078.

Despite the shallowness of $\nu_{\rm min0}$ for KIC 7747078, a unique model is derived using the χ^2 method, incorporating asteroseismic constraints and reference frequencies. To achieve a unique solution using both $\nu_{\rm min1}$ and $\nu_{\rm min0}$, it would be useful to analyse other Kepler Legacy stars that have at least two reference frequencies.

ACKNOWLEDGEMENTS

This work is supported by the Scientific and Technological Research Council of Turkey (TÜBİTAK: 123F019). We are grateful to Ege University Planning and Monitoring Coordination of Organizational Development and Directorate of Library and Documentation for their support in editing and proofreading service of this study.

DATA AVAILABILITY

The data underlying this article will be shared on reasonable request to the corresponding author.

REFERENCES

Ahlborn, F., Bellinger, E.P., Hekker, S., Basu, S., and Angelou, G.C. 2020, A&A, 639, A98 Anders, F., Chiappini, C., Rodrigues, T.S., Miglio, A., Montalbán, J., et al. 2017, A&A, 597, A30

Angulo, C., Arnould, M., Rayet, M., Descouvemont, P., Baye, D., et al. 1999, NuPhA, 656, 3

Angulo C., Descouvemont P., 2001, NuPhA, 690, 755. doi:10.1016/S0375-9474(00)00696-5 Appourchaux T., Chaplin W. J., et al., 2012, A&A, 543, A54

Arentoft T., Brogaard K., Jessen-Hansen J., Silva Aguirre V., Kjeldsen H., Mosumgaard J.R. and Sandquist E.L., 2017, ApJ, 838, 115

Asplund M., Grevesse N., Sauval A. J., Scott P., 2009, ARA&A, 47, 481. doi:10.1146/annurev.astro.46.060407.145222

Baglin A., Michel E., Auvergne M., COROT Team, 2006, in Fridlund M., Baglin A., Lochard J., Conroy L., eds, ESA Special Publication Vol. 1306, ESA Special Publication. p. 33

Ball W. H., Gizon L., 2014, A&A, 568, A123. doi:10.1051/0004-6361/201424325

Beck, P.G., Montalbán, J., Kallinger, T., De Ridder, J., Aerts, C., et al. 2012, Nature, 481, 55

Bedding, T.R., Mosser, B., Huber, D., Montalbán, J., Beck, P., et al. 2011, Nature, 471,608

Berger T. A., Huber D., van Saders J. L., Gaidos E., Tayar J., Kraus A. L., 2020, AJ, 159, 280. doi:10.3847/1538-3881/159/6/280

Brewer J.M., Fischer D.A., Valenti J.A. and Piskunov N., 2016, ApJS, 225, 32

Brown, T.M., Gilliland R.L., Noyes, R.W., Ramsey, L.W., 1991, ApJ, 368, 599

Bruntt H., Basu S., Smalley B., Chaplin, W.J., Verner, G.A., et al. 2012, MNRAS, 423, 122

Borucki W. J., Koch D., Basri G., Batalha, N., Broen, T., et al. 2010, Science, 327, 977

Böhm-Vitense E., 1958, Zeitschrift für Astrophysik, 46, 108

Çelik Orhan Z., Yıldız M., Kayhan C., 2021, MNRAS, 503, 4529. doi:10.1093/mnras/stab757

Chaplin W. J., Miglio A., 2013, ARA&A, 51, 353. doi:10.1146/annurev-astro-082812-140938

Chaplin W. J., Basu S., Huber D., Serenelli A., et al., 2014, ApJS, 210, 1

Christensen-Dalsgaard J., 1988, in Advances in Helio- and Asteroseismology, Aarhus, Denmark, July 11-17, 1986. Editors Christensen-Dalsgaard J. and Frandsen, S., IAU Symp. 123, Dordrecht: D. Reidel Publishing Co., p.295

Christensen-Dalsgaard J., 2008, ApSS, 316, 113

Cyburt R. H., Amthor A. M., Ferguson R., Meisel Z., Smith K., Warren S., Heger A., et al., 2010, ApJS, 189, 240. doi:10.1088/0067-0049/189/1/240

Çelik Orhan Z., Yıldız M., Örtel S., 2023, MNRAS, 526, 1799. doi:10.1093/mnras/stad2876

Deheuvels, S. and Michel, E. 2011, A&A, 535, A91

Deheuvels, S., Garcia, R.A., Chaplin, W.J., Basu, S., et al. 2012, ApJ, 756, 19

Deheuvels, S., Brandão, I., Silva Aguirre, V., Ballot, J., et al. 2016, A&A, 589, A93

Dupret M.-A., Thoul A., Scuflaire R., Daszyńska-Daszkiewicz J., Aerts C., Bourge P.-O., Waelkens C., et al., 2004, A&A, 415, 251. doi:10.1051/0004-6361:20034143

Ezer D., Cameron A. G. W., 1965, CaJPh, 43, 1497. doi:10.1139/p65-140

Ferguson, J.W., Alexander, D.R., Allard, F., Barmanu, T., et al. 2005, ApJ, 623, 585

Furlan E., Ciardi D.R., Cochran W.D., Everett M.E., Latham D.W., et al, 2018, ApJ, 861, 149

Gaia Collaboration, Brown A. G. A., Vallenari, A., Prusti, T., de Bruijne, J.H.J., et al., 2018, A&A, 616, A1

Gaia Collaboration, Brown A. G. A., Vallenari, A., Prusti, T., de Bruijne, J.H.J., et al., 2021, A&A, 649, A1

Giammichele N., Charpinet S., Fontaine G., Brassard P., Green E. M., Van Grootel V., Bergeron P., et al., 2018, Natur, 554, 73. doi:10.1038/nature25136

Grevesse N., Sauval A. J., 1998, SSRv, 85, 161. doi:10.1023/A:1005161325181

Huber D., Bedding T.R., Stello D., et al., 2011, ApJ, 743, 143

Iglesias C. A., Rogers F. J., 1993, ApJ, 412, 752. doi:10.1086/172958

Iglesias C.A., and Rogers F.J. 1996, ApJ, 464, 943

Jermyn A. S., Bauer E. B., Schwab J., Farmer R., Ball W. H., Bellinger E. P., Dotter A., et al., 2023, ApJS, 265, 15. doi:10.3847/1538-4365/acae8d

Kjeldsen H., and Bedding T. R. 1995, A&A, 293, 87

Kjeldsen H., Bedding T. R., Christensen-Dalsgard J., 2008, ApJL, 683, L175

Lejeune T., Cuisinier F., Buser, R., 1998, A&AS, 130, 65

Li Y., Bedding T. R., Li T., Bi S., Stello D., Zhou Y., White T.R., 2020a, MNRAS, 495, 2363

Li T., Bedding T. R., Christensen-Dalsgaard J., Stello D., Li Y., Keen M.A., 2020b, MNRAS, 495, 3431

Metcalfe T. S., Chaplin W. J., Appourchaux T., García R. A., Basu S., Brandão I., Creevey O. L., et al., 2012, ApJL, 748, L10. doi:10.1088/2041-8205/748/1/L10

Metcalfe T. S., Creevey O. L., Doğan G., et al. 2014, ApJS, 214, 27

Molenda-Zakowicz J., Sousa S.G., Frasca A., Uytterhoeven K., Briquet M. et al, 2013, MNRAS, 434, 1422

Montalbán, J., Miglio, A., Noels, A., Dupret M.-A., Scuflaire, R., and Ventura, P., 2013, ApJ, 766, 118

Mosser, B., Benomar, O., Belkacem, K., et al. 2014, A&A, 572, L5

Noll, A., Deheuvels, S. and Ballot, J. 2021, A&A, 647, A187

Paquette C., Pelletier C., Fontaine G., Michaud G., 1986, ApJS, 61, 177. doi:10.1086/191111

Paxton B., Bildsten L., Dotter A., Herwig F., Lesaffre P. and Timmes F., 2011, ApJS, 192, 35

Paxton B., Cantiello M., Arras P., Bildsten L., Brown, E.F, et al., 2013, ApJS, 208, 42

Paxton B., Marchant P., Schwab J., Bauer E. B., Bildsten L., Cantiello M., Dessart L., et al., 2015, ApJS, 220, 15. doi:10.1088/0067-0049/220/1/15

Paxton B., Schwab J., Bauer E. B., Bildsten L., Blinnikov S., Duffell P., Farmer R., et al., 2018, ApJS, 234, 34. doi:10.3847/1538-4365/aaa5a8

Paxton B., Smolec R., Schwab J., Gautschy A., Bildsten L., Cantiello M., Dotter A., et al., 2019, ApJS, 243, 10. doi:10.3847/1538-4365/ab2241

Prša A., Harmanec P., Torres G., Mamajek E., Asplund M., Capitaine N., Christensen-Dalsgaard J., et al., 2016, AJ, 152, 41. doi:10.3847/0004-6256/152/2/41

Sharma S., Stello D., Bland-Hawthorn J., Huber D., Bedding T. R., 2016, ApJ, 822, 15. doi:10.3847/0004-637X/822/1/15

Silva Aguirre, V. Ballot, J., Serenelli, A.M., and Weiss, A., 2011, A&A, 529, A63

Sullivan, P. W., Winn, J.N., Berta-Thompson, Z.K., Charbonneau, D., Deming, D., et al., 2015, ApJ, 809, 77

Tian, Z.J., Bi, S.L., Yang, W.M., Chen, Y.Q., Liu, Z.E., Liu, K., Li, T.D., Ge, Z.S., and Yu, J., 2014, MNRAS, 445, 2999

Ting Y.-S., Conroy C., Rix H.-W., Cargile P., 2019, ApJ, 879, 69. doi:10.3847/1538-4357/ab2331

Ulrich, R.K., 1986, ApJ, 306, L37

White T. R., Bedding T. R., Stello D., Christensen-Dalsgaard J., Huber D., Kjeldsen H., 2011, ApJ, 743, 161. doi:10.1088/0004-637X/743/2/161

Yıldız M., 2011, MNRAS, 412, 2571. doi:10.1111/j.1365-2966.2010.18075.x

Yıldız, M. and Çelik Orhan, Z. and Aksoy, Ç. and Ok, S., 2014, MNRAS, 441, 2148

Yıldız M., 2015, RAA, 15, 2244

Yıldız M., Çelik Orhan Z., Kayhan C., 2015, MNRAS, 448, 3689. doi:10.1093/mnras/stv295

Yıldız M., Çelik Orhan Z., Kayhan C., 2016, MNRAS, 462, 1577. doi:10.1093/mnras/stw1709

Yıldız M., Çelik Orhan Z., Kayhan, C., 2019, MNRAS, 489, 1753
Yıldız M., Örtel S., 2021, MNRAS, 504, 2273. doi:10.1093/mnras/stab996
Yıldız M., 2023, MNRAS, 518, 5552. doi:10.1093/mnras/stac3464

This paper has been typeset from a TEX/LATEX file prepared by the author.